Charge ordering transition in iron oxide Fe$_4$O$_5$ involving competing dimer and trimer formation

Sergey V. Ovsyannikov,[1,*] Maxim Bykov,[2] Elena Bykova,[1,2] Denis P. Kozlenko,[3] Alexander A. Tsirlin,[4,5] Alexander E. Karkin,[6] Vladimir V. Shchennikov,[6,7] Sergey E. Kichanov,[3] Huiyang Gou,[1,8] Artem M. Abakumov,[9,10] Ricardo Egoavil,[9] Johan Verbeeck,[9] Catherine McCammon,[1] Vadim Dyadkin,[11] Dmitry Chernyshov,[11] Sander van Smaalen,[2] and Leonid S. Dubrovinsky[1]

[1] *Bayerisches Geoinstitut, Universität Bayreuth, Universitätsstrasse 30, D-95447, Bayreuth, Germany*

[2] *Laboratory of Crystallography, Universität Bayreuth, Universitätsstrasse 30, D-95447, Bayreuth, Germany*

[3] *Frank Laboratory of Neutron Physics, JINR, 141980 Dubna, Russia*

[4] *National Institute of Chemical Physics and Biophysics, Akadeemia tee 23, 12618 Tallinn, Estonia*

[5] *Experimental Physics VI, Center for Electronic Correlations and Magnetism, Institute of Physics, University of Augsburg, 86135 Augsburg, Germany*

[6] *Institute of Metal Physics, Russian Academy of Sciences, Urals Division, GSP-170, 18 S. Kovalevskaya Str., Yekaterinburg 620041, Russia*

[7] *Institute for Solid State Chemistry of Ural Branch of Russian Academy of Sciences, 91 Pervomayskaya Str., Yekaterinburg 620990, Russia*

[8] *Key Laboratory of Metastable Materials Science and Technology, Yanshan University, Qinhuangdao 066004, China*

[9] *Electron Microscopy for Materials Research (EMAT), University of Antwerp, Groenenborgerlaan 171, B-2020 Antwerp, Belgium*

[10] *Department of Chemistry, Moscow State University, Leninskie Gory 1-3, Moscow, 119991, Russia.*

[11] *Swiss–Norwegian Beamlines at the European Synchrotron Radiation Facility, 38000, Grenoble, France*

Phase transitions that occur in materials, driven, for instance, by changes in temperature or pressure, can dramatically change their properties. Discovering new types of transitions and understanding their mechanisms is important not only from a fundamental perspective but also for practical applications. Here we investigate a recently discovered Fe$_4$O$_5$ that adopts an orthorhombic CaFe$_3$O$_5$-type crystal structure featuring linear chains of Fe ions. On cooling below ~150 K Fe$_4$O$_5$ undergoes an

unusual charge-ordering transition which involves competing dimeric and trimeric ordering within the chains of Fe ions. This transition is concurrent with a significant increase in electrical resistivity. Magnetic susceptibility measurements and neutron diffraction establish the formation of a collinear antiferromagnetic order above room temperature and a spin canting at 85 K that gives rise to spontaneous magnetization. We discuss possible mechanisms of this transition and compare it with the trimeronic charge ordering observed in magnetite below the Verwey transition temperature.

Address for correspondence:

Dr. Sergey V. Ovsyannikov
Bayerisches Geoinstitut
Universität Bayreuth
Universitätsstrasse 30
D-95447 Bayreuth
Germany
e-mail: Sergey.Ovsyannikov@uni-bayreuth.de
Phone. +49 (0) 921 55 3839
Fax. +49 (0)921 55 3769

1   Understanding unusual transformations that occur in solids, and are accompanied by peculiar

2   changes in atomic and electron structures, is important for various areas of materials science, physics

3   and chemistry[1-18]. The discovery of new phase transitions, as well as the reinvestigation of well-known

4   ones by means of more advanced characterization techniques for example can reveal unexpected

5   aspects of seemingly simple materials[2-18]. For example, the pressure-driven transformations of the

6   metallic elements lithium and sodium into insulators above ~60, and ~200 GPa, respectively[7,8] have

7   recently given a new insight into the behavior of elemental metals under high pressures. Oxides,

8   industrially important materials, also demonstrate exciting phenomena under conditions that are more

9   immediately relevant to practical applications, for instance temperature-driven 'metal–insulator'-type

10   transitions that are widely employed in various industrial settings. Understanding the mechanisms and

11   dynamics of such transitions is thus interesting both from a fundamental perspective and for

12   applications, as they can directly affect the performance of devices. Detailed reinvestigation of the

13   'metal-insulator' type transitions in some key functional materials, such as vanadium oxides, VO_2 and

14   V_2O_3 revealed a number of unexpected features and new transient states[9-15].

15   The oldest known magnetic mineral, magnetite (Fe_3O_4), adopts a cubic-spinel ($MgAl_2O_4$-type)

16   structure. Upon cooling below ~125 K it demonstrates a 'metal-insulator'-type transition, discovered

17   by Verwey in 1939, at which its electrical resistivity abruptly jumps by about two orders of magnitude[1].

18   Since Fe_3O_4 comprises both Fe^{2+} and Fe^{3+} ions, its high electrical conduction at ambient conditions is

19   attributed to a possibility of charge transfer between Fe^{2+} (charges) and Fe^{3+} (vacancies)[1,5].

20   Consequently, this transition of Fe_3O_4 to an 'insulator' phase was attributed to the charge ordering[1].

21   Only recently, more than 70 years after the discovery of this transition[1], the elusive charge ordering

22   pattern in the low-temperature phase of Fe_3O_4 has been solved by means of single-crystal X-ray

23   diffraction, and the charge ordering in magnetite was found to involve 'three-site-distortions', called

24   trimerons[2]. This picture differs drastically from the Peierls-type transition that leads to dimeric order

25   along 1D chains of metal atoms[3], signatures of which may be found in many compounds.

26   In this work, we have synthesized samples of the recently discovered Fe_4O_5[19] at high-pressure

27   high-temperature (HP-HT) conditions[20,21]. Fe_4O_5 contains equal amounts of Fe^{2+} and Fe^{3+} ions, and in

28   a similar manner to Fe_3O_4[1,2,5], it might undergo a charge ordering at relatively low temperatures. The

29   crystal structure of Fe_4O_5 comprises linear chains of octahedrally-coordinated iron ions occupying two

30   slightly different crystallographic positions, Fe2 and Fe3 and linear chains of trigonal-prismatically

31   coordinated Fe1 cations along the *a*-axis (Fig. 1a,d). Therefore, Fe_4O_5 is expected to be a good model

32   system to trace the charge-ordering process. We examined Fe_4O_5 by means of single-crystal X-ray

33   diffraction (Figs. 1,2), as well as by measurements of electronic transport properties (Fig. 3),

34 magnetization (Fig. 4), and neutron diffraction (Fig. 5), and obtained a comprehensive picture of the

35 charge-ordering transition at low temperatures.

36

37 **Results and Discussion**

38 **Crystal structure of Fe₄O₅.** At ambient conditions, Fe_4O_5 crystallizes in the orthorhombic

39 $CaFe_3O_5$-type *Cmcm* structure containing three different sites for Fe ions (Fig. 1a,d and Supplementary

40 Table 1)[19,22]. In order to evaluate the oxidation states of different Fe ions in this structure, we applied a

41 bond-valence-sum (BVS) approach (see Methods for details)[23] and found the oxidation states of Fe1,

42 Fe2, and Fe3 to be +1.92, +2.76, and +2.66, respectively. This charge distribution was confirmed by

43 electron energy loss spectroscopy (Supplementary Fig. 1). The above estimations suggest that the Fe1

44 sites are exclusively filled by Fe^{2+} ions, whereas the Fe2 and Fe3 sites are mixed-valent, featuring both

45 Fe^{2+} and Fe^{3+} ions. This picture indicates a possibility of charge transfer between Fe^{2+} and Fe^{3+} ions

46 occupying the octahedral sites, in a similar manner to other Fe-bearing oxides including magnetite[1,2].

47 Therefore, like magnetite[1], Fe_4O_5 is expected to have high concentration of charge carriers, which

48 results from high concentrations of available charges (Fe^{2+}) and vacancies (Fe^{3+}) at the octahedral sites

49 in the structure.

50 **Electronic properties of Fe₄O₅.** We examined the electronic properties of Fe_4O_5 by

51 measurements of electrical resistivity and Hall effect (see Methods) of bulk quasi-single-crystalline

52 sample (Fig. 3). The temperature dependence of the electrical resistivity $\rho(T)$ demonstrates a

53 semiconducting-like behavior (Fig. 3c) and has an activation character. That is, the resistivity is

54 lowering with temperature as function of $\rho \sim \exp[E_a/(kT)]$ (inset in Fig. 3c), where E_a is the activation

55 energy – the energy which is required to activate either the charge carriers over band gap into

56 conduction band, or the carrier mobility to enable the existing charge carriers to contribute to

57 electrical conduction, k is the Boltzmann's constant, and T is the temperature. The dramatic increase in

58 the electrical resistivity below 150 K (Fig. 3c) resembles that upon the Verwey transition in

59 magnetite[1], although the transition in Fe_4O_5 looks more continuous.

60 At ambient conditions Fe_4O_5 has an activation energy of $E_a \sim 25$ meV (inset in Fig. 3c). It is

61 interesting to note that materials with semimetal conductivity can also exhibit activation dependence

62 of electrical resistivity, e.g., magnetite demonstrated the activation energies of $E_a \sim 14$ meV[24] or 0.1

63 eV[25] in single- or polycrystalline samples, respectively. As discussed in previous works[24,26,27], the

64 charge carrier mobility in Fe_3O_4 and α-Fe_2O_3 is rather low, below ~ 0.1 cm²/(Vs), and hence, activation

65 energies should be attributed mainly to mobility activation (i.e., progressive increase in carrier

66 mobility), but not to carrier activation over band gap. Measurements of the Hall effect (see Methods) in

67 Fe_4O_5 showed a very low value at room temperature, suggesting a metallic carrier concentration above

68 10^{21} cm^{-3}, although precise estimate is not possible at the moment (Fig. 3b). The Hall effect slightly

69 increased with temperature lowering and showed ~~became unambiguously~~ positive values, suggesting

70 *p*-type conduction (Fig. 3b). It should be noted that magnetite is known to be a half-metal (that is, a

71 good conductor to electrons of one spin orientation, but semiconductor to electrons of the opposite

72 orientation)[28-30], and, taking into account certain similarities between Fe_3O_4 and Fe_4O_5, one cannot

73 exclude half-metallic conduction in Fe_4O_5, but this point requires further investigations. The low-

74 temperature phase of Fe_4O_5 has an activation energy of E_a ~113 meV suggesting an energy band gap of

75 $E_g=2E_a=0.226$ eV (Fig. 3c, inset), which is larger than reported band gap in the Verwey phase of

76 magnetite, $E_g<$~0.1 eV [31].

77 **Low-temperature crystal structure of Fe_4O_5.** On cooling below 150 K single-crystal X-ray

78 diffraction studies detected the appearance of superlattice reflections (Fig. 1b,c), i.e., the appearance of

79 a new structural order which was superimposed on the persisting initial crystal structure. Intensities of

80 these reflections grow with decreasing temperature (Supplementary Fig. 2). Indexing these superlattice

81 reflections demonstrated that this structure is incommensurately modulated, i.e., a modulated structure

82 in which atoms suffer certain periodical fluctuations from positions they would take in a hypothetical

83 'average' (basic) non-modulated structure, and a period of these fluctuations is incommensurate with

84 at least one of the periodicities in three-dimensional unit cell. These structural fluctuations in Fe_4O_5 are

85 determined by modulation wave vector, $\textbf{\textit{q}}=\sigma_1\textbf{\textit{a}}^*+\sigma_2\textbf{\textit{b}}^*$**,** where $\textbf{\textit{a}}^*, \textbf{\textit{b}}^*$ are the axes of reciprocal lattices

86 shown in Fig. 1b,c, and $\sigma_1={}^1/_3$ and temperature-dependent σ_2 are components of this vector. We solved

87 this structure and determined its superspace group as $C2_1/m(\sigma_1\sigma_20)0s$ (standard setting $P2_1/m(\sigma_1\sigma_20)0s$

88 No.11.1.2.2)[32] (Supplementary Information including *cif*-files). At 4 K, we found the lattice

89 parameters to be as follows: $a=2.8610(4)$ Å, $b=9.8123(5)$ Å, $c=12.5425(11)$ Å, $\gamma=90.0(1)$ °,

90 $V=352.10(6)$ Å^3, and $\sigma_2=0.7293(13)$ (Supplementary Table 2). The parameter $\sigma_2\approx0.7293(13)$ of the

91 modulation wave vector is irrational , and hence, a period of the structural modulations along the *b*-

92 axis cannot be proportional to the unit cell parameter *b*, – that is, the crystal structure is

93 incommensurately modulated.

94 The largest displacements of the Fe ions in the low-temperature structure of Fe_4O_5 relative to their

95 positions in the 'average' (basic) non-modulated structure were along the *a*-axis (Supplementary Fig.

96 3).Because incommensurately modulated structures cannot be visualized in crystallographic softwares,

97 to investigate the details of this low-temperature structure we used the nearest commensurately

98 modulated crystal structure with $\sigma_2=\frac{3}{4}$ (instead of σ_2~0.73), i.e., with a $\textbf{\textit{q}}$-vector $({}^1/_3,{}^3/_4,0)$

99 corresponding to '$3a\times4b\times c$' lattice (Fig. 1f). With JANA2006 software (see Methods) we plotted the

100 Fe-Fe distances and the bond-valence-sums of the Fe ions at 4 K (Fig. 2a-i). Upon cooling the lattice

101 parameters of Fe_4O_5, determined from the single-crystal X-ray diffraction data, demonstrated several

102 noteworthy features in their temperature dependencies, in particular sharp bends at 135 K, 115 K, and

103 below 90 K (Fig. 2j,k). The anomalies in the unit cell volume below 90 K resemble those reported

104 earlier for the Verwey transition in magnetite[33]. It is worthy to note that unusual electronic transitions

105 can lead to very peculiar volumetric effects — this has for example been observed with an inter-site

106 charge transfer in $LaCu_3Fe_4O_{12}$, which results in negative thermal expansion[34].

107   The main characteristics of the transition in Fe_4O_5 at 150 K involve the formation of Fe dimers

108 and trimers within the chains of Fe2 and Fe3 ions along the *a*-axis (Fig. 1f), while the chains of ferrous

109 Fe1 ions were only weakly modulated along the *c*-axis (Supplementary Fig 3). A constant Fe1-Fe1

110 distance in the low-temperature structure (~2.861 Å at 4K) (Fig. 2a) served as a reference point, which

111 enabled us to conclude about the dramatic shortening of some Fe2-Fe2 and Fe3-Fe3 distances (Fig. 1f,

112 marked by elongated ellipsoids, and Figs 2b,c). As seen in Fig. 1f each chain of Fe2 or Fe3 ions

113 contains either dimers or trimers, and as seen from Fig. 2b,c, the overall numbers of dimers and trimers

114 throughout the crystal structure are roughly equal.

115   Using data of Fe-O bond lengths at 4 K (Supplementary Fig. 4 and Table 3) we estimated the

116 bond-valence-sums (Fig. 2g-i). We noticed that a small non-equivalence in these bond-valence-sums

117 between the Fe2 and Fe3 sites found at 295 K (+2.76 *vs* +2.66, respectively) persisted in the low-

118 temperature phase too (Fig. 2h,i). This fact hints that the charge carriers (Fe^{2+}) have slight preference

119 to the Fe3 sites, and for this reason the Fe3 chains could be less charged than the Fe2 ones (Fig. 2h,i).

120 It is also seen from comparison of the bond-valence-sums of dimers and trimers in the Fe2 and Fe3

121 chains (Fig. 1h). The bond-valence-sums analysis shows that the trimers are, in general, composed of

122 one Fe^{2+} and two Fe^{3+} ions (Fig. 1h), similar to the trimerons in Fe_3O_4[2]. Likewise, the Fe ions in the

123 dimers in the Fe3 chains have an oxidation state close to +2.5, i.e., the dimers are Fe^{2+}–Fe^{3+} pairs with

124 one shared electron. However, the dimers in the Fe2 chains look a bit overcharged – their average

125 charge, +5.35, is notably higher than that of the dimers in the Fe3 chains, +5.1 (Fig. 1h). Meanwhile,

126 as seen from comparison of Fig. 2h and Fig. 2i, the charge density waves along the Fe2 and Fe3 chains

127 are in opposite phases of modulation, thereby suggesting nearly uniform charge distribution in the

128 lattice. In contrast to these intricate changes in the Fe2 and Fe3 chains across the phase transition, the

129 bond-valence-sums of the Fe1 ions (Fig. 2g) and the distances between them (Fig. 2a) remained equal,

130 thereby demonstrating that the low-temperature transition is driven by the charge ordering, and hence,

131 the Fe1 chains remain inactive in this transition.

132   As can be seen in Fig. 2d-f, the minimal Fe1-Fe2, Fe2-Fe3, and Fe1-Fe3 distances at T=4 K do not

133   exhibit any dramatic shortening along the c- and b-axes when compared with the aforementioned

134   reference distance of ~2.861 Å. This fact indicates that the transition in Fe_4O_5 can be considered as a

135   quasi-1D charge ordering in the Fe2 and Fe3 chains, leading to the formation of both dimers in some

136   chains, and trimers in the others (Fig. 1f). Each 1D chain has an individual set of the Fe-Fe distances

137   obeying the three-fold period ($\sigma_I={}^1/_3$). X-ray diffraction images collected below 150 K show an

138   appreciable diffuse scattering (Supplementary Fig. 5) that could be related to additional structural

139   effects on the local level, but those go beyond the scope of our present work.

140   **Magnetic properties of Fe_4O_5.** Magnetic properties of Fe_4O_5 were examined by magnetic

141   susceptibility and neutron diffraction studies on bulk polycrystalline samples. We observed weak

142   ferromagnetism up to room temperature, with the remnant magnetization of ~0.02 μ_B/Fe at 300 K (Fig.

143   4d). This behaviour resembles hematite (α-Fe_2O_3), which is a weak ferromagnet with a tiny magnetic

144   moment of ~0.002 μ_B/Fe at room temperature[35] because of the weak spin canting (i.e., tilting of spins

145   by small angle about their axis) on top of the collinear antiferromagnetic ordering. This resemblance

146   suggests that it may be the case in Fe_4O_5 as well. A more pronounced and clearly intrinsic

147   ferromagnetic signal is seen below ~90 K (Fig. 4a,b,c), and at 2 K the magnetization saturates to ~0.2

148   μ_B/Fe (Fig. 4d). Thus, these data indicate that below 85-90 K Fe_4O_5 is a canted antiferromagnet, i.e.,

149   antiferromagnet in which the spins are tilted by small angle about their axis and do not fully

150   compensate each other that leads to such non-zero magnetic moment. The abrupt growth in the

151   magnetization below 90 K (Fig. 4a,b,c) correlates with the anomaly detected in the lattice parameters

152   below 90 K (Fig. 2j,k).

153   Neutron diffraction showed the presence of magnetic order already at room temperature. This

154   magnetic order resulted in the growth of the (021) peak at $d = 4.51$ Å that has a negligible contribution

155   from the nuclear structure (Fig. 5a). Magnetic moments of the Fe ions are directed along the c-axis and

156   ordered antiferromagnetically (Fig. 5b,c). Note that from the powder data we can neither exclude nor

157   confirm a weak spin canting. To reduce the number of refinable parameters, we constrained the

158   ordered magnetic moments of the Fe ions located at different sites to be equal. From temperature

159   dependencies of magnetic moments, we estimated the antiferromagnetic transition temperature as

160   T_N~320 K (Fig. 5b). Near 150 K, we detected an abrupt increase in average ordered magnetic moment

161   by ~0.5 μ_B (Fig. 5b). This effect correlates with the structural modulation and ensuing changes in

162   electronic density distribution. Near T_{SC}=85 K, we found another magnetic transition that was

163   attributed to spin canting of the ordered magnetic moments towards the a-axis (Fig. 5d). This re-

164   arrangement in the magnetic structure resulted in the appearance of ferromagnetic components (M_x-

165 FM) that gave rise to two magnetic peaks, (002) at d=6.19 Å and (022) at d=d 3.81 Å (Fe1 and Fe2

166 sublattices) and contributed to the (020) nuclear peak at d=4.84 Å (Fe3 sublattice). The ferromagnetic

167 components of the Fe1 and Fe2 magnetic sublattices are antiparallel, and thus, compensate each other

168 (Fig. 5d). In contrast, the ferromagnetic component of the Fe3 sublattice remains uncompensated, and

169 this leads to the remnant magnetization observed below T_{SC} (Fig. 4).

170   The lattice of Fe_4O_5 was found to exhibit very different axial compressibilities (Fig. 2j). The

171 magnetic order can give insight into these peculiarities. Thus, negative thermal expansion along the b-

172 axis (Fig. 2j) may be related to the antiferromagnetic spin arrangement along this direction (Fig. 5c,d).

173 Antiparallel spins will generally tend to increase the antiferromagnetic exchange energy by expansion

174 of Fe−Fe distances and, hence, by increasing Fe−O−Fe angles that play a crucial role in this

175 superexchange. Similar effects were reported for CuF_2[36] and $SrCu_2(BO_3)_2$[37]. Progressive shrinkage

176 along the a-axis with temperature decreasing (Fig. 2j) suggests an enhancing role of a-axis in the

177 charge transfer and Fe-Fe interactions at lower temperatures and could explain the quasi-1D character

178 of the transition.

179   **The low-temperature transition.** The charge ordering in Fe_4O_5 is preceded by the magnetic

180 transition that imposes ferromagnetic spin arrangement along the a-direction (Fig. 5d). The electronic

181 configuration of Fe^{2+} ions is $3d^6$, so that in the high-spin state five electrons adopt one spin direction,

182 and the sixth electron adopts the opposite spin direction, forming the minority-spin channel. Below the

183 Verwey transition temperature, the spins of Fe atoms forming trimerons in Fe_3O_4 are aligned

184 ferromagnetically[33,38], and the minority-spin electron of one Fe^{2+} ion can be shared with two

185 neighbouring Fe^{3+} ions[2]. This process is facilitated by weak axial distortion of FeO_6 octahedra that

186 introduces an additional crystal-field splitting and defines position of the lowest-energy t_{2g} orbital

187 hosting this minority-spin electron of Fe^{2+}. Then, three atoms sharing the same plane of this lowest-

188 energy orbital form a trimeron[2]. Thus, the charge-ordering pattern is related to connectivity of FeO_6

189 octahedra.

190   The ferromagnetic order along the a-direction renders a similar mechanism operative in Fe_4O_5.

191 Both the Fe2 and Fe3 octahedra in Fe_4O_5 showed a noticeable axial compression that splits the three t_{2g}

192 levels of Fe ions in regular FeO_6 octahedron into the lower-lying singlet and higher-lying doublet. The

193 lowest-energy orbital that can be occupied by the minority-spin electron lies in plane, which is shared

194 by all octahedra of one chain (Fig. 1e,g). The same plane is also shared by two contiguous chains, and

195 together they form a structural ribbon comprising one Fe2 chain encompassed by two Fe3 chains (Fig.

196 1g). Alternation of dimers and trimers throughout the crystal structure may be understood by

197 considering such diagonal ribbons (Fig. 1e,g), in which two chains form the trimers and one chain

forms the dimers, or the other way around. Notice, that dimers (D) are always formed in the space 'between' trimers (T), as illustrated in Fig. 1g. For the opposite case of 'D-T-D' ribbons, which for example surround this selected 'T-D-T' ribbon (Fig. 1e), the dimers in the Fe3 chains are always formed in the space 'between' trimers in the central Fe2 chain (see 3-5 upper chains in Fig. 1f). The simultaneous formation of dimers and trimers and their nearly perfect alternation in these ribbons might be linked, for instance, to peculiar bonding of O1 oxygen atoms shared by the Fe2 and Fe3 chains (Fig. 1g). If only dimers or only trimers are formed, these O1 oxygen atoms (labeled by arrows in Fig. 1g) might become "overbonded" (i.e., their electrical charge might become higher than 2) or "underbonded" (i.e., with an electrical charge smaller than 2), respectively. Other factors, such as elastic coupling between Fe2 and Fe3 chains through O1 atoms, located between these chains within each ribbon, could also affect the ordering pattern. Thus, the formation of dimers in the space 'between' trimers partly compensates the lattice distortions arising from the formation of trimers (Fig. 1f,g).

Conclusions

In summary, we showed that at 150 K Fe_4O_5 undergoes a phase transition involving the simultaneous formation of dimers and trimers within linear chains of octahedrally-coordinated Fe ions. This unexpected charge ordering gives rise to unusual modulations in the crystal structure. The underlying mechanism of the charge ordering in Fe_4O_5 may be, to some extent, similar to that in magnetite[2], but the different nature of the crystal structure results in the formation of not only trimers but also dimers, present in approximately equal numbers throughout the crystal structure. Unlike, the Verwey transition in magnetite which has 3D character,[2] the charge ordering in Fe_4O_5 looks as quasi-1D transition. It is worth mentioning a case of Fe_2OBO_3 in which a charge ordering involving the ordering of localized charges without formation of any units (dimers, trimers, etc) also led to incommensurate phase.[39] The coexistence of dimers and trimers in Fe_4O_5 at low temperatures may be related to peculiar structural connectivity and elastic coupling between Fe chains.

Methods

Preparation and characterization of Fe₄O₅. The samples of Fe_4O_5 were synthesized in 1200-tonne Multi-Anvil Presses at BGI. We explored several synthesis routes to fabricate this polymorph. The best and simplest path we found was a direct synthesis from a mixture of Fe_3O_4 (Aldrich, 99.99% purity) and Fe (99.99%) corresponding to Fe_4O_5 stoichiometry at conditions of 11-14 GPa and 1000-1300 °C. We employed a standard assembly, which included a Re capsule, $LaCrO_3$ heater, W3Re/W25Re

231 thermocouples and an octahedral container[40]; the procedure was similar to that described before[20,21].

232 Typical synthesis times were about 1-4 hours. This Fe_4O_5 polymorph is readily recoverable at ambient

233 conditions and remains (meta)-stable if not overheated above 150 °C[41]. It is stable also under

234 application of high pressure at least up to 40 GPa[19,42]. The chemical composition of the samples was

235 examined by scanning electron microscopy (SEM) with a LEO-1530 instrument and by microprobe

236 analysis with a JEOL JXA-8200 electron microprobe. The purity and the stoichiometry of the samples

237 were verified. We can note here that doped modifications of Fe_4O_5 may be also routinely prepared

238 from magnetite (e.g., those reported doped with Cr and Mg)[43-45].

239   The sample for transmission electron microscopy investigation was prepared by crushing the

240 material, dispersing it in ethanol and depositing it onto a holey carbon grid. Electron energy loss

241 spectroscopy (EELS) measurements were performed using a FEI Titan[3] 80-300 transmission electron

242 microscope operated at 300 kV. A monochromator was used to optimize the energy resolution for the

243 EELS measurements to 250 meV. The EELS spectra were fitted using the EELSMODEL program

244 (www.eelsmodel.ua.ac.be)[46]. EELS of the Fe-$L_{2,3}$ excitation edge combined with model based fitting to

245 reference spectra for Fe^{2+} and Fe^{3+} was used to measure the oxidation state of the Fe cations. We

246 obtained a mixed valence condition of 53(4) % Fe^{2+} and 47(4) % Fe^{3+}. Details on the collection

247 treatment of the EELS spectra are given in Supplementary information (Supplementary Fig. 1).

248   ***Single-crystal X-ray diffraction studies of Fe₄O₅.*** At ambient conditions the crystal structure of

249 Fe_4O_5 was determined from single-crystal X-ray diffraction (XRD) studies using a four-circle Oxford

250 Diffraction Xcalibur diffractometer ($\lambda = 0.71073$ Å) equipped with an Xcalibur Sapphire2 CCD

251 detector (details are available in Supplementary Information). Then, high quality single crystals were

252 selected for temperature-dependent single-crystal X-ray diffraction studies. In one experiment we

253 studied temperature-dependent X-ray diffraction using a Mar345dtb diffractometer equipped with a

254 MAR345 image plate detector from 295 to 80 K. For the lattice parameter determination, the series of

255 phi scans (60 frames, $\Delta\varphi = 1°$, exposure time = 60 s/°) were measured at different temperatures and

256 processed with the CrysAlisPro software package. It should be noted that for each temperature point

257 the same part of reciprocal space was covered, thus giving equal sets of diffraction peaks used for the

258 orientation matrix refinement. Another experiment with full data collection was carried out at SNBL

259 (The Swiss-Norwegian Beam Line, ESRF, Grenoble, France) with a wavelength of 0.6884 Å at the

260 lowest temperature 4 K. Intensity data were collected on a single-axis diffractometer equipped with a

261 Pilatus 2M pixel detector by 360° φ scans ($\Delta\varphi = 1°$). Data processing (peak intensities integration,

262 background evaluation, cell parameters, and absorption correction) was done with the CrysAlisPro

263 171.36.28 program. The structure was solved by *SUPERFLIP*[47] employing charge-flipping algorithm

264 in superspace. Structure refinements were performed with the JANA2006 crystallographic computing
265 system[48].

266 In order to evaluate the oxidation states of different Fe ions in the crystal structure we applied a
267 bond-valence-sums (BVS) method,[23] which is based on analysis of Fe-O bond lengths around the Fe
268 ions. In this method the oxidation state of an ion (V_i) is a sum of all its bond valences (S_{ij}), each of
269 those is determined as: $S_{ij} = \exp[(R_{ij} - d_{ij})/b_0]$, where, d_{ij} is the distance between atoms i and j, R_{ij} is the
270 empirically determined distance for this cation-anion pair, and b_0 is an empirical parameter which is
271 normally about 0.37 Å[23].

272 ***Measurements of electronic transport and magnetic properties of Fe$_4$O$_5$.*** Electronic transport
273 properties (Fig. 2) were measured by the conventional Montgomery method using an Oxford
274 Instruments setup. We measured temperature dependencies of electrical resistivity and Hall effect. The
275 Hall effect consists in the appearance of voltage difference in the direction perpendicular to both
276 electrical current in a conductor and applied magnetic field, which is also directed perpendicular to this
277 electrical current.

278 Magnetic susceptibility (Fig. 3) was measured with a Quantum Design MPMS SQUID
279 magnetometer in the temperature range 2–380 K in applied fields up to 5 T under both field-cooling
280 (FC) and zero-field-cooling (ZFC) conditions.

281 ***Neutron diffraction studies of Fe$_4$O$_5$.*** The magnetic structure of Fe$_4$O$_5$ was studied using a DN-12
282 neutron diffractometer for studies of microsamples[49] at the IBR-2 high-flux pulsed reactor (FNLP
283 Dubna, Russia). The sample with a volume about 1.5 mm^3 was placed inside the CCR-based cryostat.
284 The neutron powder diffraction data were collected at scattering angles $2\theta = 45.5$ and 90°. The
285 measurements were performed in the temperature range $10 - 300$ K. The data were analyzed by the
286 Rietveld method using the Fullprof program[50]. Possible models of magnetic structure were considered
287 taking into account the symmetry analysis performed by BasIreps program
288 (https://www.ill.eu/sites/fullprof/).

1. Verwey, E. J. W. Electronic conduction of magnetite (Fe_3O_4) and its transition point at low temperatures. *Nature* **144**, 327-328 (1939).
2. Senn, M. S., Wright, J. P. & Attfield, J. P. Charge order and three-site distortions in the Verwey structure of magnetite. *Nature* **481**, 173-176 (2012).
3. Peierls, R. E. Quantum Theory of Solids, Oxford University Press, London, 1955.
4. Mott, N. F. Metal-insulator transition. *Rev. Mod. Phys.* **40**, 677-683 (1968).
5. Mott, N. F. *Metal–insulator transitions* (London, Taylor and Francis Ltd, 1974).
6. Imada, M., Fujimori, A. & Tokura, Y. Metal insulator transitions. *Rev. Mod. Phys.* **70**, 1039-1263 (1998).
7. Matsuoka, T. & Shimizu, K. Direct observation of a pressure-induced metal-to-semiconductor transition in lithium, *Nature* **458**, 186-189 (2009).
8. Ma, Y. *et al.* Transparent dense sodium. *Nature* **458**, 182-185 (2009)
9. Limelette, P. *et al.* Universality and Critical Behavior at the Mott Transition. *Science* **302**, 89-92 (2003).
10. Qazilbash, M. M. *et al.* Mott transition in VO_2 revealed by infrared spectroscopy and nano-imaging. *Science* **318**, 1750-1753 (2007).
11. Nakano, M. *et al.* Collective bulk carrier delocalization driven by electrostatic surface charge accumulation. *Nature* **487**, 459-462 (2009).
12. Driscoll, T. *et al.* Memory metamaterials, *Science* **325**, 1518-1521 (2009).
13. Lupi, S. *et al.* A microscopic view on the Mott transition in chromium-doped V_2O_3. *Nat. Comm.* **1**, 105 (2010).
14. Budai, J. D. *et al.* Metallization of vanadium dioxide driven by large phonon entropy. *Nature* **515**, 535-539 (2014).
15. Morrison, V. R. *et al.* A photoinduced metal-like phase of monoclinic VO_2 revealed by ultrafast electron diffraction. *Science* **346**, 445-448 (2014).
16. de Jong, S. *et al.* Speed limit of the insulator–metal transition in magnetite. *Nature Mater.* **12**, 882-886 (2013).
17. Neaton, J. B. & Ashcroft, N.W. Pairing in dense lithium. *Nature* **400**, 141–144 (1999).
18. Neaton, J. B. & Ashcroft, N. W. On the constitution of sodium at higher densities. *Phys. Rev. Lett.* **86**, 2830–2833 (2001).
19. Lavina, B. *et al.* Discovery of the recoverable high-pressure iron oxide Fe_4O_5. *Proc Nat. Acad. Sci. US* **108**, 17281-17285 (2011).
20. Ovsyannikov, S. V. *et al.* Perovskite-like Mn_2O_3: a path to new manganites. *Angew. Chem. Int. Ed.* **52**, 1494-1498 (2013).
21. Ovsyannikov, S. V. *et al.* A hard oxide semiconductor with a direct and narrow bandgap and switchable *p-n* electrical conduction. *Adv. Mater.* **26**, 8185-8191 (2014).
22. Gerardin, R., Millon, E., Brice, J. F., Evrard, O. & Le Caer, G. Transfert lectronique d'intervalence entre sites inequivalants: etude de $CaFe_3O_5$ par spestrometrie Müssbauer. *J. Phys. Chem. Solids* **46**, 1163-l 171 (1985).
23. Brese, N. E. & O'Keffee, M. Bond-valence parameters for solids. *Acta Cryst*. **B47**, 192-197 (1991).
24. Shchennikov, V. V., Ovsyannikov, S. V., Karkin, A. E., Todo, S. & Uwatoko, Y. Galvanomagnetic properties of fast neutron bombarded Fe_3O_4 magnetite: A case against charge ordering mechanism of the Verwey transition. *Solid State Commun.* **149**, 759-762 (2009).
25. Morris, E. R. & Williams. Q., Electrical resistivity of Fe_3O_4 to 48 GPa: compression-induced changes in electron hopping at mantle pressures. *Journal of Geophysical Research* **102**, 139-148 (1997).
26. Morin, F. J. Electrical properties of α-Fe_2O_3. *Phys. Rev.* **93**, 1195-1199 (1954).

27. Ovsyannikov, S. V., Morozova, N. V., Karkin, A. E. & Shchennikov, V. V. High-pressure cycling of hematite α-Fe$_2$O$_3$: Nanostructuring, *in situ* electronic transport, and possible charge disproportionation. *Phys. Rev. B* **86**, 205131 (2012).

28. Dedkov, Y. S., Rüdiger, U. & Güntherodt, G. Evidence for the half-metallic ferromagnetic state of Fe$_3$O$_4$ by spin-resolved photoelectron spectroscopy. *Phys. Rev. B* **65**, 064417 (2002).

29. Fonin, M., Dedkov, Yu. S., Pentcheva, R., Rüdiger, U. & Güntherodt, G. Magnetite: a search for the half-metallic state. *J. Phys.: Condens. Matter* **19**, 315217 (2007).

30. Müller, G. M. *et al.* Spin polarization in half-metals probed by femtosecond spin excitation. *Nat. Mater.* **8**, 56-61 (2009).

31. Chainani, A., Yokoya, T., Morimoto, T., Takahashi, T. & Todo, S. High-resolution photoemission spectroscopy of the Verwey transition in Fe$_3$O$_4$. *Phys. Rev. B* **51**, 17976 –17979 (1995).

32. Stokes, H. T., Campbell, B. J. & van Smaalen, S. Generation of (3+d)-dimensional superspace groups for describing the symmetry of modulated crystalline structures. *Acta Crystallogr. A.* **67**, 45-55 (2011).

33. Wright, J. P., Bell, A. M.T. & Attfield J. P. Variable temperature powder neutron diffraction study of the Verwey transition in magnetite Fe$_3$O$_4$. *Solid State Sciences* **2**, 747 –753 (2000).

34. Long, Y. W. *et al.* Temperature-induced A–B intersite charge transfer in an *A*-site-ordered LaCu$_3$Fe$_4$O$_{12}$ perovskite. *Nature* **458**, 60-63 (2009).

35. Morin, F. J. Magnetic susceptibility of α-Fe$_2$O$_3$ and α-Fe$_2$O$_3$ with added titanium. *Phys. Rev.* **78**, 819-820 (1950).

36. Chatterji, T. & Hansen, T. C. Magnetoelastic effects in Jahn–Teller distorted CrF$_2$ and CuF$_2$ studied by neutron powder diffraction. *J. Phys.: Condens. Matter* **23,** 276007 (2011).

37. Vecchini, C. *et al.* Structural distortions in the spin-gap regime of the quantum antiferromagnet SrCu$_2$(BO$_3$)$_2$. *J. Solid State Chem.* **182**, 3275–3281 (2009).

38. Walz, F. The Verwey transition—a topical review. *J. Phys. Condens. Matter* **14**, R285–R340 (2002).

39. Angst, M. *et al.* Incommensurate Charge Order Phase in Fe$_2$OBO$_3$ due to Geometrical Frustration. *Phys. Rev. Lett.* **99,** 256402 (2007).

40. Frost, D. J. *et al.* A new large-volume multianvil system, *Phys. Earth Planet. Inter.* **143– 144**, 507-514 (2004).

41. Woodland, A. B., Frost, D. J., Trots, D. M., Klimm, K. & Mezouar, M. *In situ* observation of the breakdown of magnetite (Fe$_3$O$_4$) to Fe$_4$O$_5$ and hematite at high pressures and temperatures, *Amer. Mineral.* **97**, 1808-1811 (2012).

42. Kothapalli, K. *et al.* Nuclear forward scattering and first-principles studies of the iron oxide phase Fe$_4$O$_5$, *Phys. Rev. B* **90**, 024430 (2014).

43. Woodland, A. B. *et al.* Fe$_4$O$_5$ and its solid solutions in several simple systems. *Contrib. Miner. Petrol.* **166**, 1677-1686 (2013).

44. Ishii, T. *et al.* High-pressure phase transitions in FeCr$_2$O$_4$ and structure analysis of new post-spinel FeCr$_2$O$_4$ and Fe$_2$Cr$_2$O$_5$ phases with meteoritical and petrological implications. *Am. Mineral.* **99**, 1788–1797 (2014).

45. Guignard, J. & Crichton, W. A. Synthesis and recovery of bulk Fe$_4$O$_5$ from magnetite, Fe$_3$O$_4$. A member of a self-similar series of structures for the lower mantle and transition zone. *Mineralogical Magazine.* **78**, 361-371 (2014).

46. Verbeeck, J. & Van Aert, S. Model based quantification of EELS spectra, *Ultramicroscopy* **101**, 207-224 (2004).

47. Palatinus, L. & Chapuis, G. *SUPERFLIP* – a computer program for the solution of crystal structures by charge flipping in arbitrary dimensions. *J. Appl. Crystallogr.* **40**, 786-790 (2007).

48. Petricek, V., Dusek, M. & Palatinus, L. Crystallographic Computing System JANA2006: General features. *Zeitschrift Für Krist. – Cryst. Mater.* **229**, 345-352 (2014).

49. Aksenov, V. L. *et al.* DN-12 time of flight high pressure neutron spectrometer for investigation of microsamples. *Physica B.* **265**, 258-262 (1999).
50. Rodriguez-Carvajal, J. Recent advances in magnetic structure determination by neutron powder diffraction. *Physica B:Cond. Matter* **192**, 55-69 (1993).

Acknowledgements

Author contributions

S.V.O. synthesized and characterized the Fe_4O_5 samples. M.B., E.B., S.v.S., V.D., and D.C. performed the single crystal X-ray diffraction study at low temperatures. M.B. and S.v.S. resolved the structure of the new low-temperature phase. S.E.K. performed the neutron diffraction measurements. D.P.K. analyzed the neutron diffraction data and derived magnetic structure models. A.A.T. measured the magnetic properties. A.E.K. and V.V.S. measured the electronic transport properties. H.G. synthesized the samples and discussed the results. A.M.A., R.E., and J.V. collected and analyzed the EELS spectra. D.P.K., A.M.A., A.A.T, and C.M. discussed the magnetic properties and contributed to manuscript writing. S.V.O. wrote a first draft of the manuscript, and all the co-authors read, revised and commented on that. S.V.O. and L.S.D. initiated and designed the research.
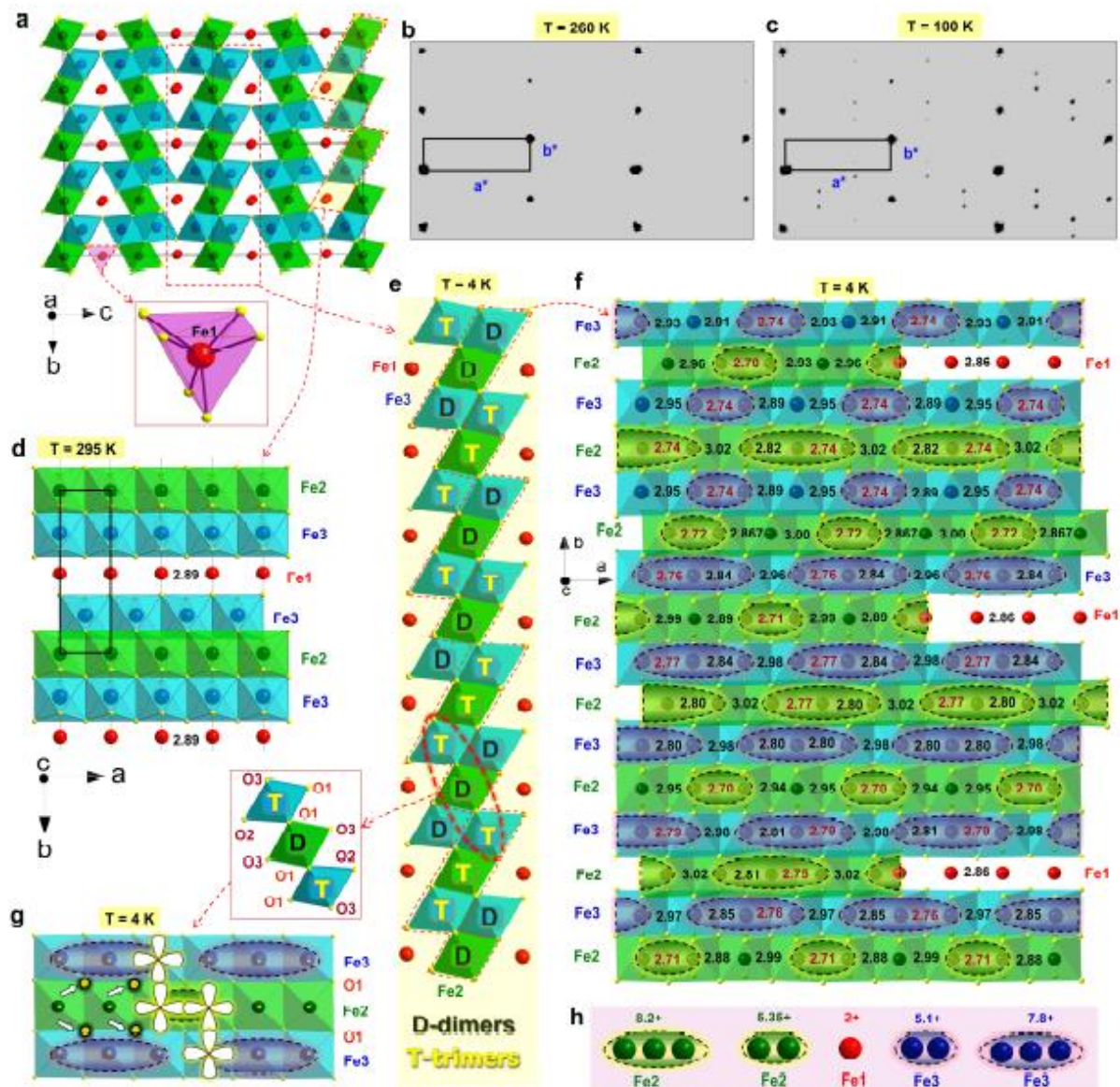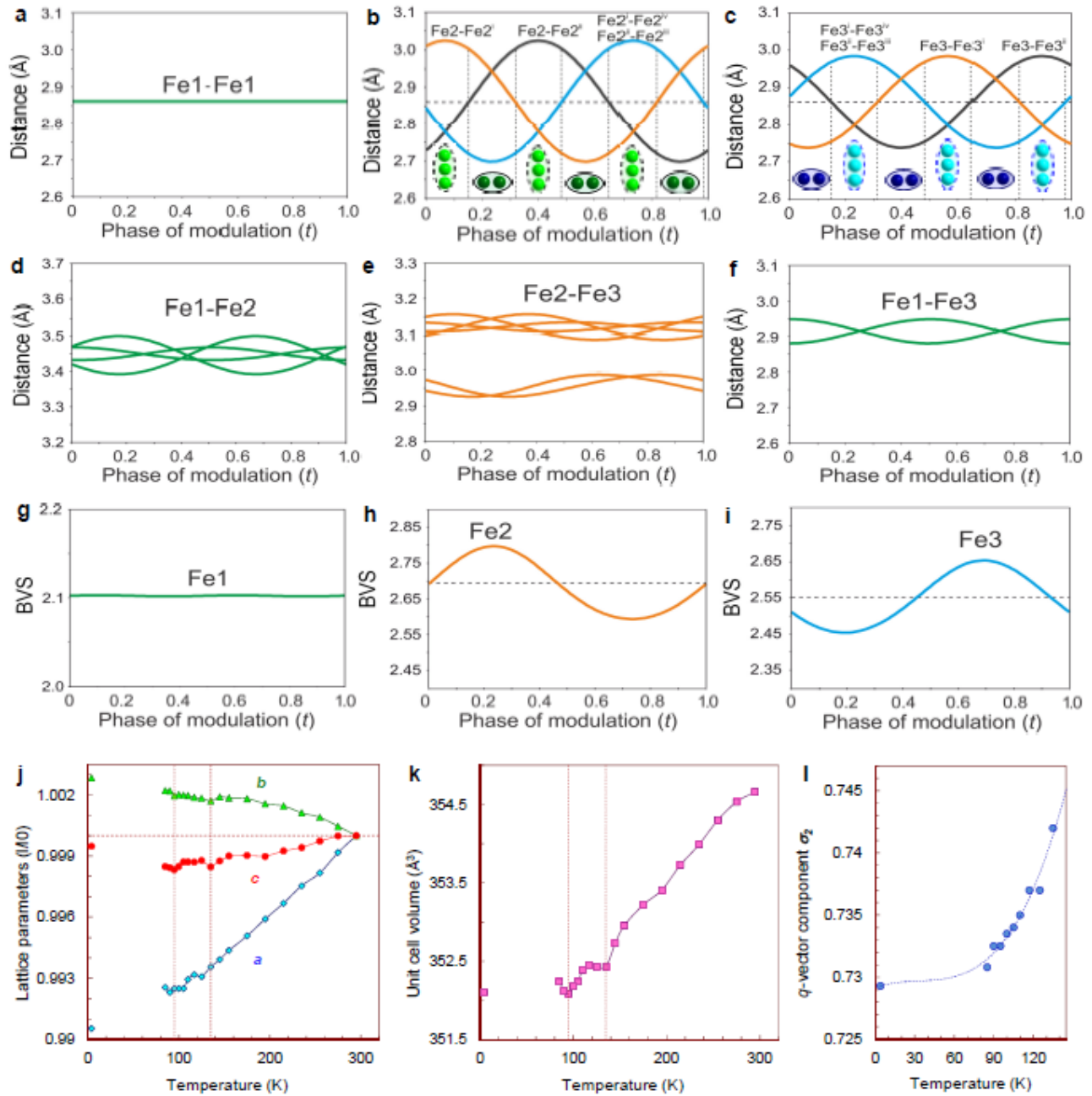
Figure 1. Crystal structure of Fe₄O₅. **a**, Crystal structure projected down the *a*-axis at room temperature. Red spheres, trigonal-prismatically coordinated Fe1 cations; green and blue spheres, octahedrally coordinated ions occupying two slightly different Fe2 and Fe3 crystallographic sites, respectively. The trigonal prismatic coordination environment of the Fe1 cations is shown as purple prism (below). **b,c**, Examples of reciprocal lattices of X-ray diffraction intensities at 260 K (**b**) and 100 K (**c**). *a** and *b** are the axes of reciprocal lattices. **d**, Crystal structure in projection of the *c*-axis at room temperature. The bold rectangle shows the unit cell. The numbers indicate the distances in Å units between the neighboring Fe ions along the *a*-axis. **e,f**, The same part of the low-temperature crystal structure at 4 K in approximation of the nearest commensurate '*3a×4b×c*' superstructure shown

in two projections along the *a*-axis (**e**) and *c*-axis (**f**). These plots demonstrate the preference to dimeric (D) or trimeric (T) ordering in different chains. In (**f**) we give only one of each couple of the parallel Fe3 chains plotted in (**e**) because in this projection they overlap each other, and the red dashed line in (**e**) indicates which chains are selected for (**f**). In three lines we show as examples the parts of both the Fe1 and Fe2 chains which always overlap each other in this projection. The numbers are distances between the closest Fe ions in Å units. The shortest distances in this structure are highlighted in red colour. All the Fe1-Fe1 distances are the same (~2.861 Å). [**g**, Example of three-chain ribbon with shared edges highlighted by a dashed ellipsoid in (**e**). Upper inset in (**g**) labels all the oxygen atoms of this ribbon. The O1 oxygen sites (marked by arrows) that neighbor the central ions in the trimers might be potentially "underbonded". The electron *d*-orbitals of the Fe ions within such planes have the same spatial symmetry (as examples *d*-orbitals of four Fe ions are shown in white colour). **h**, Typical bond valence sums (BVS) of the dimers and trimers at 4 K.

Figure 2. Crystal structure parameters of Fe_4O_5. a-f, The closest distances between the Fe ions calculated from the crystal structure at 4 K: Fe1-Fe1 (**a**), Fe2-Fe2 (**b**), Fe3-Fe3 (**c**), Fe1-Fe2 (**d**), Fe2-Fe3 (**e**), and Fe1-Fe3 (**f**). The reference distance, Fe1-Fe1 ~ 2.861 Å, is shown in (**b,c**) as a horizontal dashed line. The upper indexes in (**b,c**) denote different symmetry codes: (i) $x+1,y,z$; (ii) $x-1,y,z$; (iii) $x-2,y,z$; (iv) $x+2,y,z$, where x, y, and z are the axes. These plots demonstrate the formation of dimers (one short and two long distances) and trimers (two short and one long distances) in the Fe2 and Fe3 chains. We labeled these areas at the plots by visual representations. One can see in (**b,c**) that the distances between the Fe ions in the dimers and trimers can smoothly vary through the crystal structure. **g,h,i,**

Bond valence sums (BVS) of the Fe ions at 4 K: Fe1 (**g**), Fe2 (**h**), and Fe3 (**i**). **j,k,l** Temperature dependencies of lattice parameters (**j**), unit cell volume (**k**), and incommensurate q-vector component, σ_2 (**l**). The data in (**j-l**) represent a combination of results of two experiments from 300 down to 80 K and at 4 K. The vertical dashed lines indicate two crossovers.
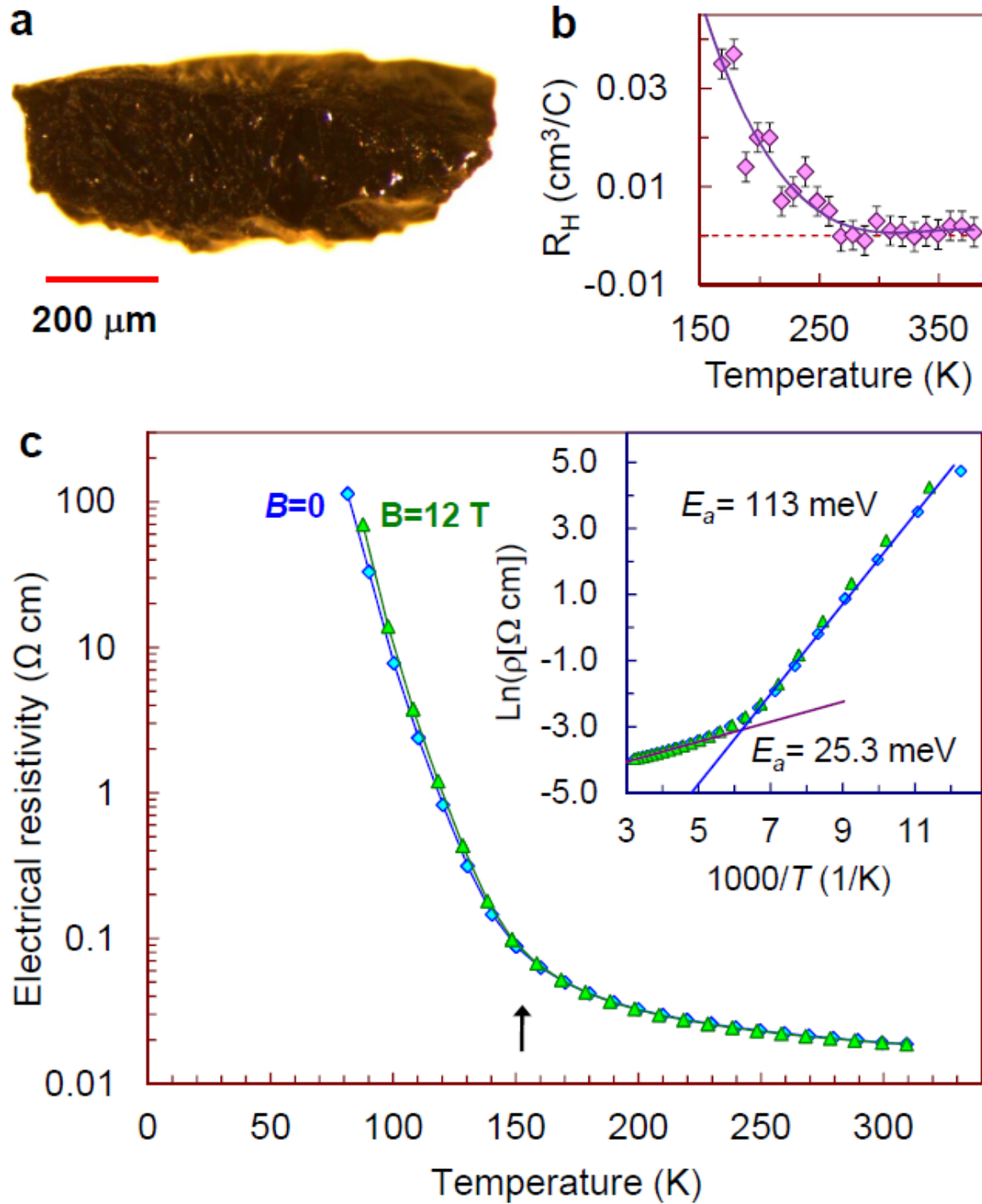

Figure 3. **Electronic properties of Fe$_4$O$_5$. a**, A photograph of a large quasi-single-crystal of Fe$_4$O$_5$. **b**, Temperature dependence of the Hall constant, R_H measured in magnetic field of 12 T (the

error bars show potential average uncertainties related to a noise contribution to the signal, experimentally determined for several temperature points). . We note that, in a similar way to Fe_3O_4[24] and Fe_2O_3[27], the measured Hall effect of Fe_4O_5 might also include some contribution of the extraordinary Hall effect arising from non-zero magnetization in applied magnetic field; but investigation of this effect was beyond the scope of our present work. **c**, Temperature dependence of electrical resistivity of Fe_4O_5 at zero and 12 T magnetic field. This curve exhibits a bend at 150 K (marked by arrow), indicating a transition between the states with high- and low electrical conduction (i.e., of 'metal-insulator' type). The inset in (**c**) shows determination of the activation energies, E_a in the both phases. The activation energies of these states were found to be E_a=25.3 and 113 meV above and below 150 K, respectively. We note that the electrical resistivity curves (**c**) show a noticeable positive magnetoresistance effect below 150 K, but this effect requires further investigations and that goes beyond the scope of this work.
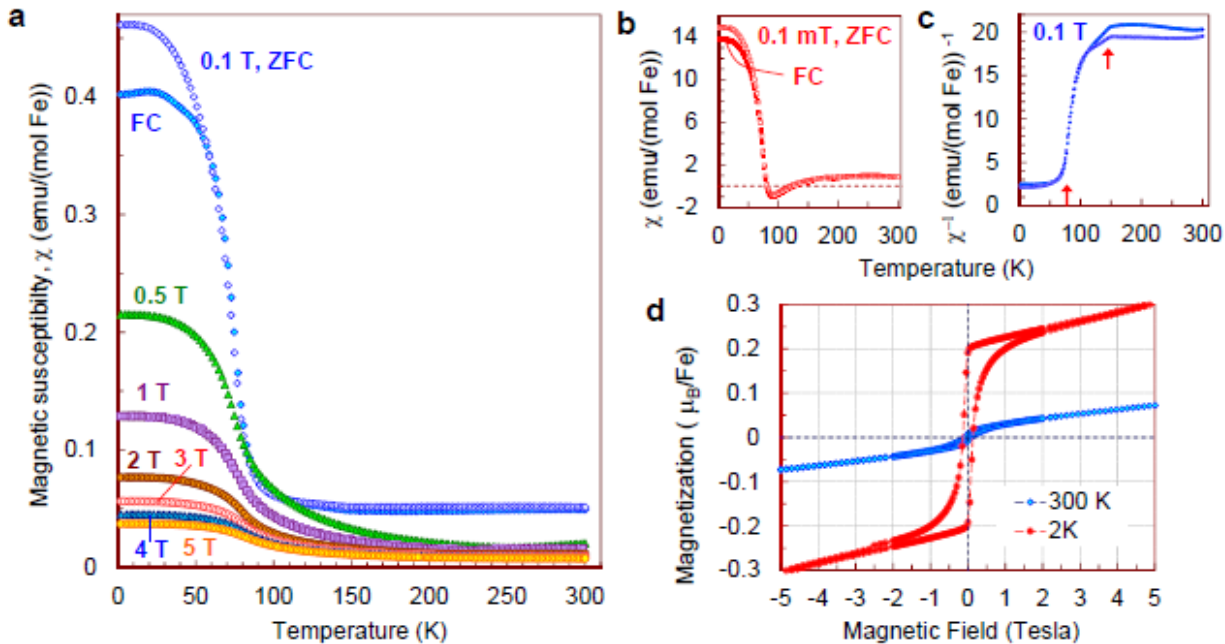
Figure 4. Magnetic properties of Fe_4O_5. a, Temperature dependencies of magnetic susceptibility χ of Fe_4O_5 measured at different magnetic fields. ZFC and FC correspond to zero-field cooling and field-cooling, respectively. **b**, Temperature dependencies of the magnetic susceptibility measured in magnetic field of 0.1 mT. **c**, Reciprocal magnetic susceptibility measured in magnetic field of 0.1 T from (**a**). These curves indicate two crossovers, near 150 K and 75 K. A weak downturn around 150 K marks the structural and electronic phase transitions (Fig. 3c). **d**, Magnetization curves measured at 2 K and 300 K. Notice, that these magnetic studies were performed on bulk polycrystalline samples, and

hence, we cannot exclude the presence of a minor impurity of unreacted Fe_3O_4 that would also induce weak ferromagnetic behavior.
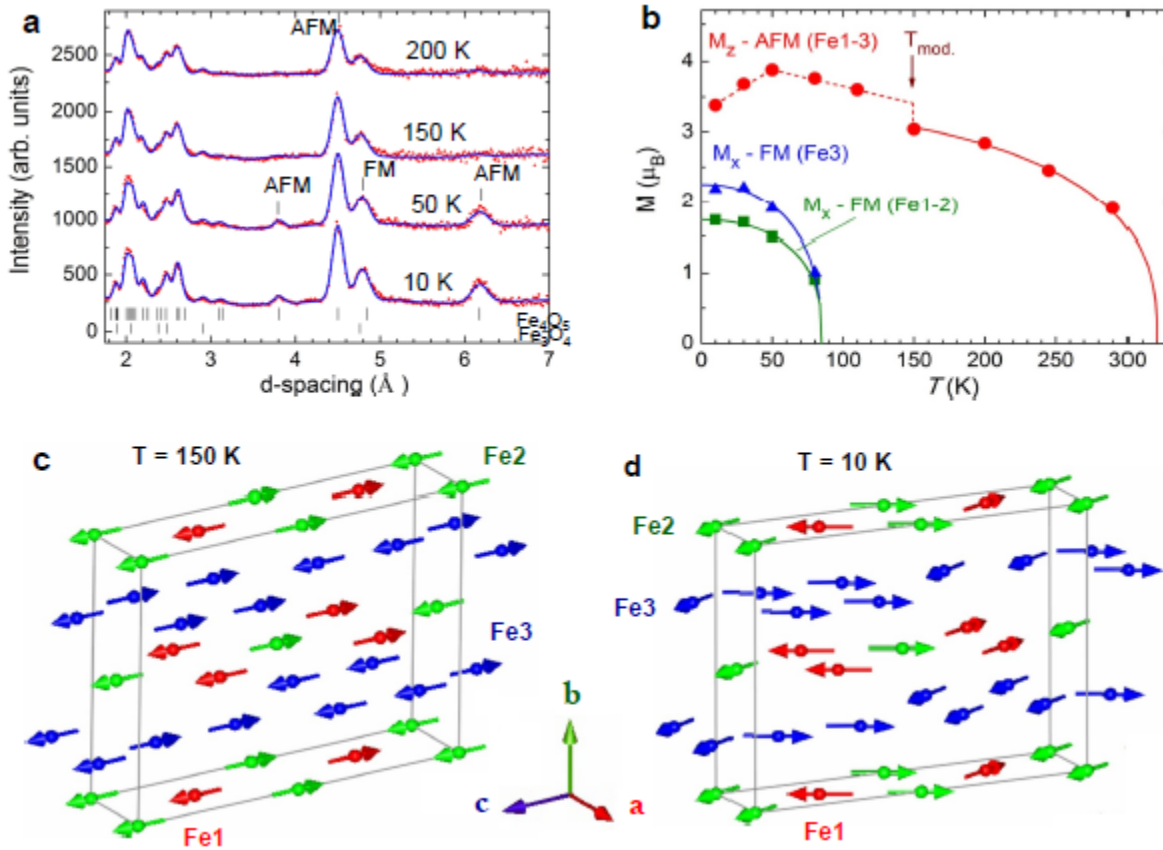
Figure 5. Magnetic structure of Fe₄O₅. a, Temperature evolution of neutron diffraction patterns of Fe_4O_5. The dashes in the lower part of the plot correspond to the expected reflection positions for Fe_4O_5 (upper row) and Fe_3O_4 (lower row). **b**, Temperature dependencies of the average M_z (AFM, antiferromagnetic) and M_x (FM, ferromagnetic) components of the Fe spins. These dependencies demonstrate two effects as follows: (*i*) the spin canting below $T_{SC} = 85$ K from *c*- towards *a*-axis, and (*ii*) an abrupt increase in the ordered magnetic moment at lattice modulation temperature, $T_{mod} = 150$ K. **c,d**, Long-range magnetic order in Fe_4O_5 above (**c**) and below (**d**) the spin canting temperature. The arrows indicate the orientations of the Fe spins in different crystallographic positions, of which labels and colours correspond to those in Fig. 1. For simplicity we show the unit cell edges corresponding to the crystal structure at ambient conditions. In the actual incommensurate low-temperature structure the Fe ions are slightly shifted (Figs. 1f, 2a-c).

Supplementary Information

Charge ordering transition in iron oxide Fe_4O_5 involving competing dimer and trimer formation

Sergey V. Ovsyannikov*, Maxim Bykov, Elena Bykova, Denis P. Kozlenko, Alexander A. Tsirlin, Alexander E. Karkin, Vladimir V. Shchennikov, Sergey E. Kichanov, Huiyang Gou, Artem M. Abakumov, Ricardo Egoavil, Johan Verbeeck, Catherine McCammon, Vadim Dyadkin, Dmitry Chernyshov, Sander van Smaalen, and Leonid S. Dubrovinsky

*corresponding author: e-mails: sergey.ovsyannikov@uni-bayreuth.de, sergey2503@gmail.com

Table of Content of this PDF-file:

Supplementary Figures:

Supplementary Tables:

Figure S1. Typical Electron Energy Loss Spectrum collected at 295 K showing the Fe-L$_{2,3}$ edge for Fe$_4$O$_5$. A decomposition of the spectrum into a linear combination of the Fe^{2+} (FeTiO$_3$) and Fe^{3+} (α-Fe$_2$O$_3$) contributions is shown. For clarity, the fitted curve and the experimental spectrum are multiplied by a factor of 2.
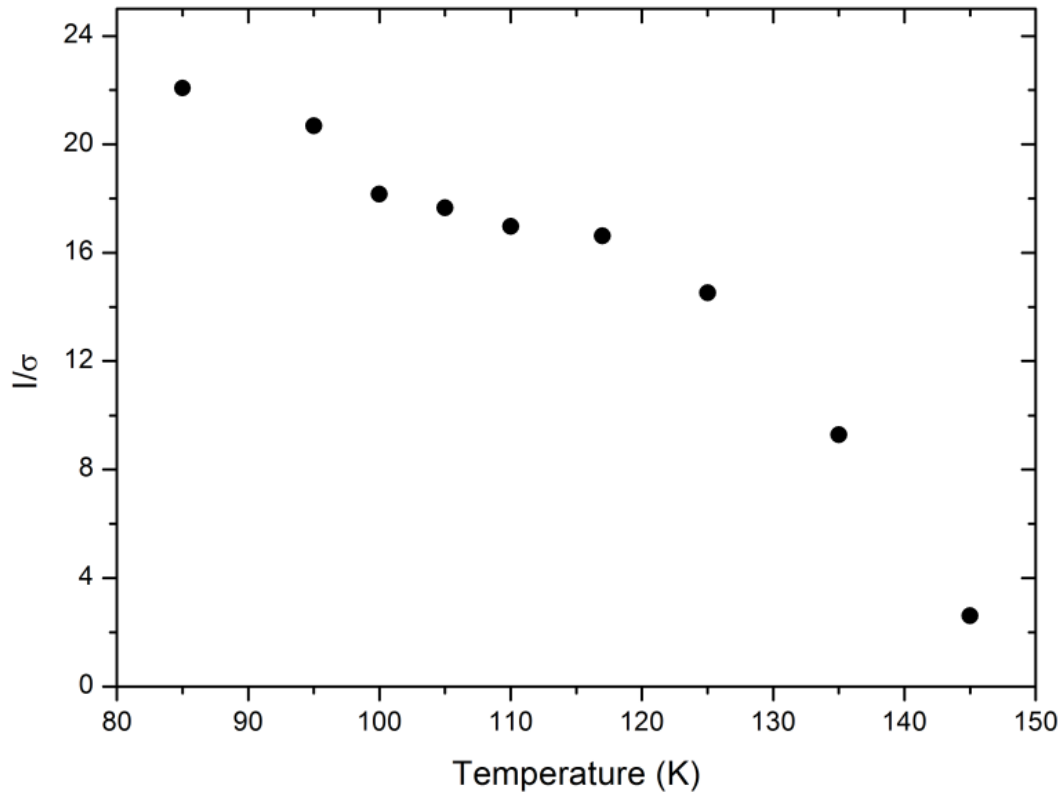
Figure S2. Temperature dependence of intensity of the superlattice reflections in the low-temperature incommensurate crystal structure of Fe_4O_5 on cooling below 150 K. We could detect the appearance of these additional superlattice reflections in single-crystal diffraction images of Fe_4O_5 only at temperatures below 150 K. The intensities of these reflections were gradually increased with decreasing temperature and tend to a saturation below 120 K.
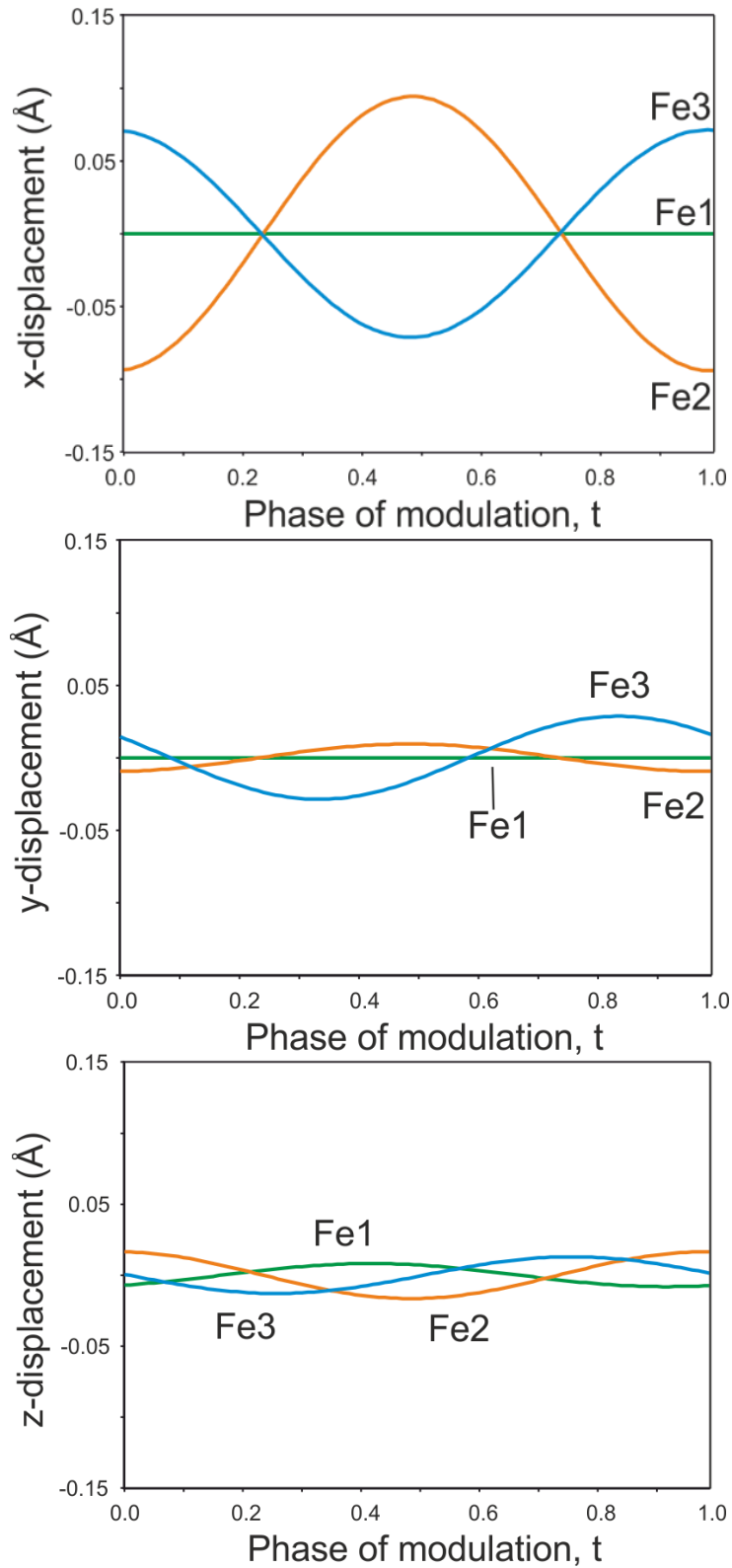
Figure S3. Selected *t*-plots showing the displacements of atoms in the low-temperature incommensurately modulated crystal structure of Fe_4O_5 at 4 K from their positions in the basic non-modulated crystal structure. One can see that the chains of the ferrous Fe1 ions were only weakly modulated, and the largest amplitude of changes in their position being only 0.01 Å

along the *c*-axis.
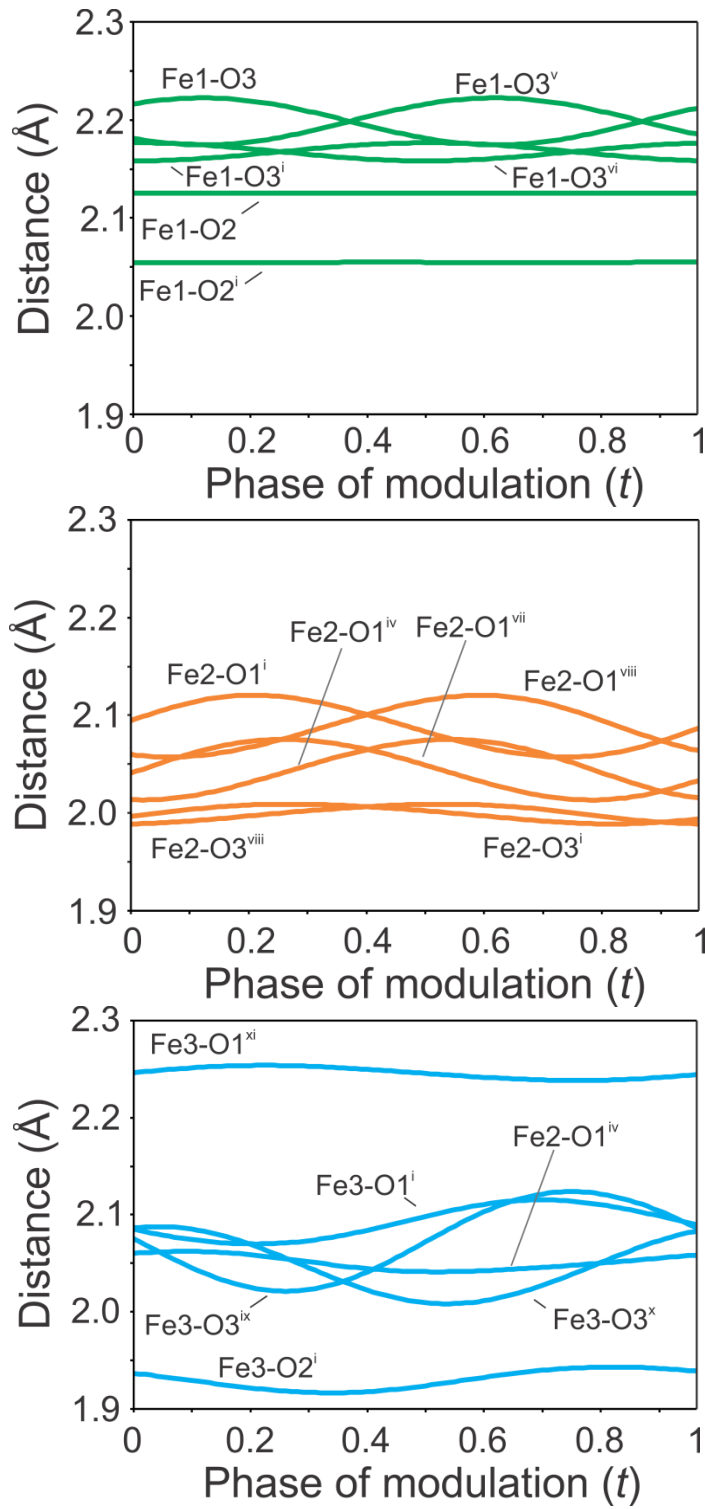
Figure S4. t-plots showing the Fe-O distances in the low-temperature incommensurately modulated crystal structure of Fe_4O_5 at 4 K. The upper indexes (*i*) – (*xi*) mean different symmetry codes: (*i*) $x+1$, y, z; (*ii*) $x-1$, y, z; (*iii*) $x-2$, y, z; (*iv*) $x+2$, y, z; (*v*) x, y, $-z+^1/_2$; (*vi*) $x+1$, y, $-z+^1/_2$; (*vii*) - $x+^1/_2$,-$y+^1/_2$, z; (*viii*) $-x+^3/_2$, $-y+^1/_2$, z; (*ix*) $x+^1/_2$, $y+^1/_2$, z; (*x*) $x+^3/_2$, $y+^1/_2$, z; (*xi*) $-x+1$, $-y+1$, z.
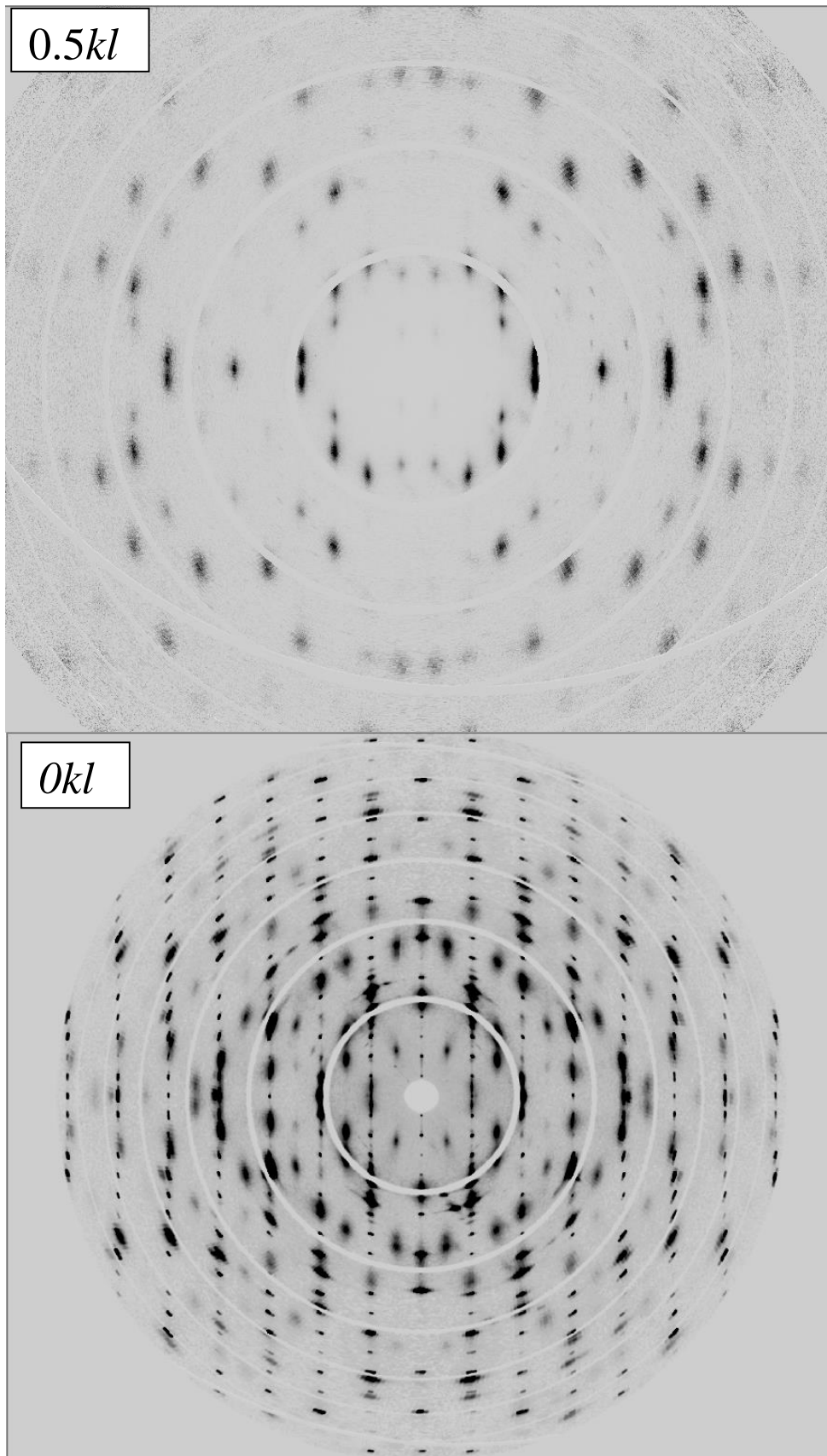
Figure S5. Diffuse scattering in the low-temperature incommensurately modulated crystal structure of Fe_4O_5 at 4K. The diffuse scattering was observed on *hkl* (h = 0.5, 1, 1.5 …) planes.

1kl

2kl
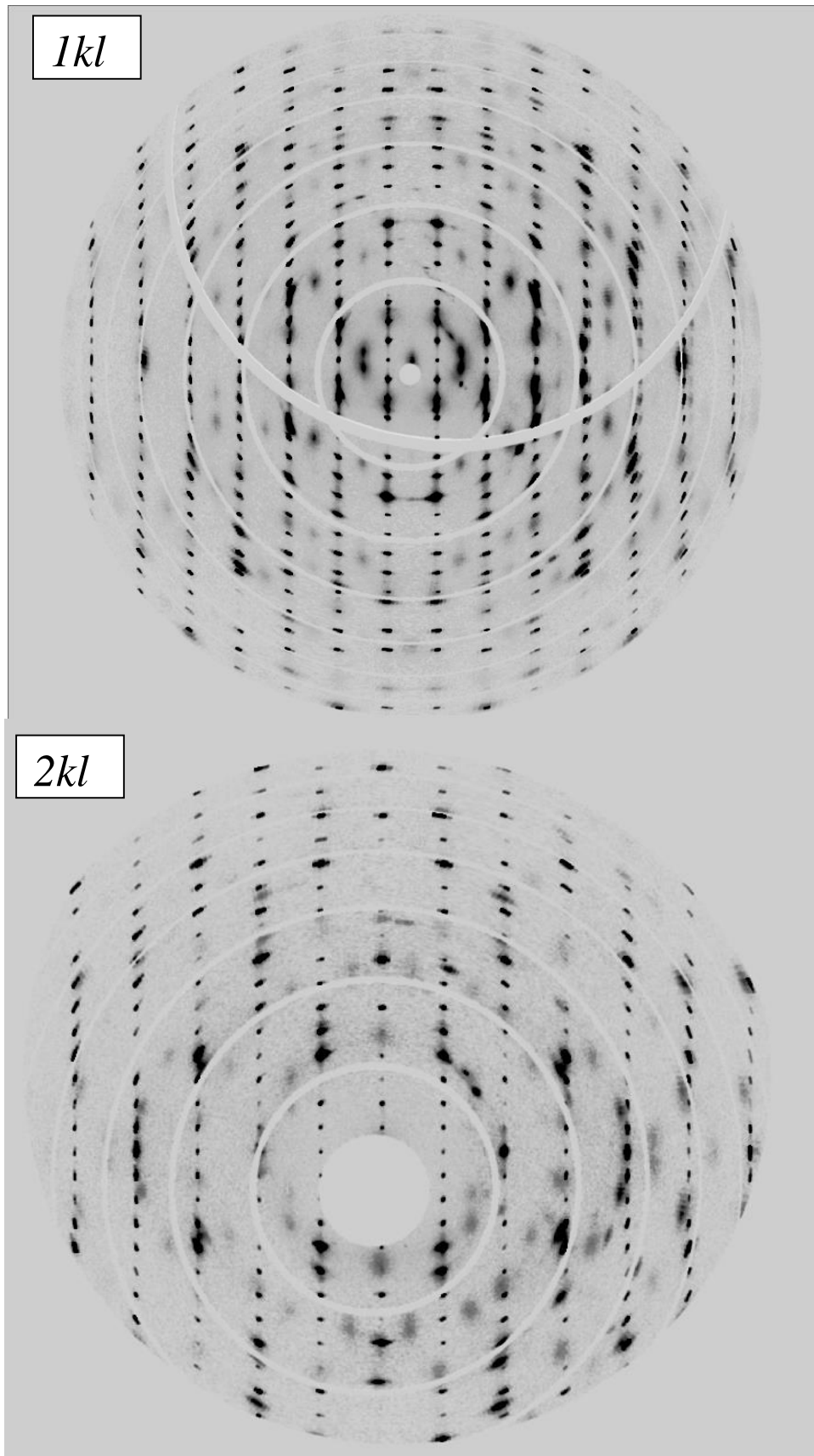
Figure S5. (continued).

Table S1. Unit cell parameters of Fe_4O_5 at 295 K.

Formula			Fe_4O_5	
Space group			Orthorhombic *Cmcm* (#63)	
Lattice parameters (Å)			a=2.8906(1), b=9.8024(3), c=12.5804(4)	
Unit cell volume (Å^3)			356.46(2)	
Formula units in the cell, Z			4	
Calculated density (g/cm^3)			5.65306	

Atom	Seat	Atomic coordinates			Isotropic displacements
		x/a	y/b	z/c	U_{eq} Å^2
Fe1	4c	0	0.50518(6)	$1/4$	0.01199(13)
Fe2	4a	0	0	0	0.00859(12)
Fe3	8f	0	0.26037(4)	0.11742(4)	0.00894(11)
O1	8f	0	0.3590(2)	0.54417(2)	0.0101(3)
O2	4c	0	0.1601(3)	$1/4$	0.0082(4)
O3	8f	0	0.0930(2)	0.64222(2)	0.0090(3)

*U_{eq} is defined as one third of the trace of the orthogonalized U^{ij} tensor.

These parameters have been determined in a single-crystal X-ray diffraction study on a four-circle Oxford Diffraction Xcalibur diffractometer ($\lambda = 0.71073$ Å). $R_1 = 0.0321$, $wR_2 = 0.0631$ for all data.

Table S2. Parameters of the crystal structure refinement of the low-temperature phase of Fe_4O_5 at 4 K.

Crystal data	
Empirical formula	Fe_4O_5
Formula weight, $g \cdot mol^{-1}$	303.38
a, Å	2.8610(4)
b, Å	9.8123(5)
c, Å	12.5425(11)
γ, °	90.0(1)
V, Å^3	352.10(6)
Z	4
Density, $g \cdot cm^{-3}$	5.7212
Space group	$C2_1/m(\sigma_1\sigma_20)0s$
q-vector	(0.3332(5), 0.7293(13), 0)
Data collection	
Temperature, K	4
Wavelength, Å	0.6884
$(\sin\Theta/\lambda)_{max}$	0.757
R_{int}	0.0275
Main reflections $(I>3\sigma(I))$/all	450/456
Satellite reflections $(I>3\sigma(I))$/all	1154/1786
Redundancy	3.145
Structure refinement	
Number of parameters	59
R_{all} $(I>3\sigma(I))$	0.0518
$R_{main}(I>3\sigma(I))$	0.0426
R_{sat} $(I>3\sigma(I))$	0.0837
wR_{all}	0.0850
wR_{main}	0.0790
wR_{sat}	0.0978

Table S3. Selected Fe-Fe distances in the low-temperature crystal structure of Fe₄O₅ at 4 K.

Given are minimal (d_{min}), maximal (d_{max}) and averaged distances (d_{ave}).

	d_{min}, Å	d_{max}, Å	d_{ave}, Å
Fe1 – Fe1	2.861(10)	2.861(10)	2.861(10)
Fe2 – Fe2	2.630(11)	2.978(11)	2.860(11)
Fe3 – Fe3	2.671(11)	2.967(11)	2.861(11)
Fe1 – Fe2	3.432(3)	3.468(3)	3.450(3)
Fe1 – Fe3	2.8803(8)	2.9487(8)	2.9144(7)
Fe2 – Fe3	2.9257(8)	2.9874(8)	2.9574(8)

Table S4. Structural parameters for the low-temperature incommensurate phase of Fe₄O₅ at 4 K.

Atomic coordinates are given with respect to the average non-modulated unit cell. The crystal structure in the superspace is defined by the coordinates of the atoms in the basic structure and their displacements. So, the position of the atom μ can be obtained as a sum of its position in the basic structure ($\bar{\mathbf{X}}(\mu)$) and the value of the modulation function $\mathbf{u}^{\mu}(\bar{x}_4)$, where $\bar{x}_4 = t + \mathbf{q} \cdot \bar{\mathbf{X}}(\mu)$. Atomic modulation functions $\mathbf{u}^{\mu} = \left(u_x^{\mu}, u_y^{\mu}, u_z^{\mu}\right)$ were described by first-order Fourier series:

$u_i^{\mu}(\bar{x}_4) = A_i(\mu)\sin(2\pi\bar{x}_4) + B_i(\mu)\cos(2\pi\bar{x}_4)$, where $i = x, y, z$.

	Fe1	Fe2	Fe3	O1	O2	O3
x/a	0.75117(3)	0.25	0.2495(2)	-0.2610(11)	0.2337(15)	0.2434(9)
y/b	0.25510(5)	0.25	0.51083(4)	0.39105(17)	0.4103(3)	0.15859(18)
z/c	0.25	0	0.11781(3)	0.04391(15)	0.25	0.14238(15)
U_{eq}, Å²	0.0071(2)	0.0067(2)	0.0071(2)	0.0063(4)	0.0058(5)	0.0070(4)
A_x, Å	0	-0.0941(6)	0.0278(3)	-0.0014(14)	0	-0.0166(14)
B_x, Å	0	0	-0.0656(4)	0.0100(17)	0	0.0077(14)
A_y, Å	0	-0.0094(5)	0.0278(3)	0.0339(16)	0	-0.0275(15)
B_y, Å	0	0	-0.0071(4)	0.0433(15)	0	-0.0112(15)
A_z, Å	-0.0065(5)	0.0166(6)	0.0125(4)	0.0132(19)	-0.0123(25)	-0.0036(19)
B_z, Å	0.0049(5)	0	0.0030(4)	0.0203(19)	-0.0093(25)	0.0090(19)